33 Near-bottom boundary layers

ALEJANDRO SOUZA (ajso@pol.ac.uk) and
CARL FRIEDRICHS (cfried@vims.edu)

33.1 Steady and oscillating boundary layers

33.1.1 Introduction

Currents on the continental shelf are influenced to a greater or lesser extent by the effect of friction at the seabed. In deep water with slow currents, the boundary layer in which frictional forces act occupies a relatively thin region near the bed, whereas, in shallow water with faster currents, it may occupy the entire water depth and dominate the dynamics (Soulsby, 1983).

Generally speaking, the turbulence energy and shear stress decay from their maximum values near the bottom to zero at the outer edge of the boundary layer. Following Soulsby (1983), the boundary layer can be subdivided into three different layers. The first is the bed layer, the region of thickness a few centimeters very close to the bed, where either molecular viscosity dominates or the presence of roughness can cause changes in the turbulence profile. The second is the logarithmic layer; this layer is a few meters thick in the sea and it is the region where the local dynamics are not affected either by the nature of the free-stream flow or by the detail of the bed and it has a simple universal form. The third is the outer layer, the layer above the logarithmic layer, in which the velocity and turbulence profiles depend strongly on the nature of the free-stream flow. In the shelf seas the free-stream flow is usually due to a combination of various types of forcing, including tidal oscillations, the Earth's rotation, and density currents. In this section we will briefly discuss the logarithmic layer and then we will discuss in more detail the outer layer for planetary, oscillatory, and planetary–oscillatory flows.

33.1.2 The logarithmic layer

Near the bed the effects of inertia and rotation can be neglected compared with those of friction and the flow behaves like a steady flow. In a steady uniform non-stratified flow we can postulate the existence of a range of heights that is simultaneously sufficiently far above the bed that the geometry of the bed roughness elements is unimportant and sufficiently far below the surface that the water depth is unimportant, in determining the flow characteristics. Within this range of heights the velocity gradient depends only on the bed shear stress τ_0, the water density ρ, and the height above the bed z (Soulsby, 1990). In this layer the molecular viscosity is unimportant and the turbulent eddy viscosity can be regarded as a function of true physical quantities. From this we have

$$\frac{\mathrm{dU}}{\mathrm{dz}} \propto \frac{1}{z}\left(\frac{\tau_0}{\rho}\right)^{1/2}. \tag{33.1}$$

In terms of the friction velocity we can rewrite this as

$$\frac{\mathrm{dU}}{\mathrm{dz}} = \frac{u_*}{\kappa z}, \tag{33.2}$$

where κ is von Kármán's constant. The velocity profile is then obtained by integrating with respect to z and applying the boundary condition $U = 0$ at the non-zero height $z = z_0$:

$$U(z) = \frac{u_*}{\kappa}\ln\left(\frac{z}{z_0}\right), \tag{33.3}$$

where the roughness length z_0 is directly related to the nature of the seabed (for a full derivation, see Jackson [1981]). This logarithmic velocity profile has been observed in nature and this approach has been used as part of the boundary conditions in many numerical models applying a slip condition, like in Davies (1986), where

$$\tau_0 = \rho k U^2 \tag{33.4}$$

so that

$$k = \left(\frac{\kappa}{\ln(z/z_0)}\right)^2, \tag{33.5}$$

where z is the reference height above the seabed at which k and the bed current are computed, commonly 1 m.

In numerical models boundary conditions for the turbulence energy E or q^2, using a slip condition, usually assume a steady state (Baumert and Radach, 1992), $\partial E/\partial t = 0$. So that vertical diffusion of momentum and any buoyancy effects are neglected, a production–dissipation balance is applied so that the boundary conditions for E and q^2 are

$$E = \frac{u_*^2}{C_\mu^{1/2}}, \qquad q^2 = B_1^{2/3}u_*^2, \tag{33.6}$$

where C_μ and B_1 are constants from the closure scheme (see Galperin *et al*. [1988]).

33.1.3 The planetary boundary layer

The first frictional boundary-layer model in a rotating frame was presented by Ekman (1905) in his classic

Marine Turbulence: Theories, Observations, and Models. Results of the CARTUM Project, ed. Helmut Baumert, John Simpson, and Jürgen Sündermann. Published by Cambridge University Press.

paper. He showed that the influence of the Earth's rotation on a steady current flowing over the sea bottom will be to cause the current and the shear stress to veer anticyclonically with distance from the bed, merging with the geostrophic flow at the outer edge of the boundary layer. Hence the equations of momentum for a current driven by a steady pressure gradient in the presence of friction are

$$\begin{aligned} fu &= -\frac{1}{\rho}\frac{\partial P}{\partial y} + N_z \frac{\partial^2 v}{\partial z^2}, \\ -fv &= -\frac{1}{\rho}\frac{\partial P}{\partial x} + N_z \frac{\partial^2 u}{\partial z^2}. \end{aligned} \tag{33.7}$$

From the above it can be seen that there are two forces acting to accelerate the fluid, the one due to the horizontal pressure gradients and the one due to the vertical stress. So the velocities of the two different forcings can be considered separately. So we will have the geostrophic velocity forced by the pressure gradients, which for simplicity we will consider in the x direction only, so that

$$u_{\mathrm{g}} = -\frac{1}{\rho f}\frac{\partial P}{\partial y} \tag{33.8}$$

and the velocity due to the vertical stress which is termed the Ekman velocity in honour of Ekman's pioneering work on boundary-layer theory. So the Ekman velocity satisfies

$$\begin{aligned} fu_{\mathrm{E}} &= N_z \frac{\partial^2 v_{\mathrm{E}}}{\partial z^2}, \\ -fv_{\mathrm{E}} &= N_z \frac{\partial^2 u_{\mathrm{E}}}{\partial z^2} \end{aligned} \tag{33.9}$$

with boundary conditions

$$(u_{\mathrm{E}}, v_{\mathrm{E}}) = (0, 0) \tag{33.10}$$

at the edge of the boundary layer and

$$(u_{\mathrm{E}}, v_{\mathrm{E}}) = \left(-u_{\mathrm{g}}, 0\right) \tag{33.11}$$

at the bottom, so that

$$\begin{aligned} u_{\mathrm{E}} &= u_{\mathrm{g}} \mathrm{e}^{-z/\delta_{\mathrm{E}}} \sin\left(\frac{z}{\delta_{\mathrm{E}}}\right), \\ v_{\mathrm{E}} &= -u_{\mathrm{g}} \mathrm{e}^{-z/\delta_{\mathrm{E}}} \cos\left(\frac{z}{\delta_{\mathrm{E}}}\right), \end{aligned} \tag{33.12}$$

where

$$\delta_{\mathrm{E}} = \left(\frac{2N_z}{f}\right)^{1/2} \tag{33.13}$$

is the layer thickness within which the stress acts and is usually referred as the Ekman-layer thickness.

33.1.4 Boundary layers for oscillatory flows

In this case we will not consider the flow in the immediate vicinity of the bed, but we will consider the bottom boundary condition to be at the interface between the logarithmic layer and the Ekman layer.

The equation of momentum for an oscillatory flow in a vertically homogeneous channel is

$$\frac{\partial u}{\partial t} = -g\frac{\partial \zeta}{\partial x} + \frac{\partial}{\partial z}\left(N_z \frac{\partial u}{\partial z}\right), \tag{33.14}$$

where u is the velocity along the x axis, ζ is the surface elevation, t is time, g is the gravitational acceleration, ρ is the density, and N_z is the eddy viscosity, which will be considered constant for simplicity. If we limit the motion to a single harmonic with frequency ω (i.e. a single tidal component), then, following Prandle (1982a), we can find the following solution:

$$u(z,t) = \mathrm{Re}\left\{U(z)\mathrm{e}^{\mathrm{i}\omega t}\right\} \tag{33.15}$$

and

$$\zeta(t) = \mathrm{Re}\left\{W\mathrm{e}^{\mathrm{i}\omega t}\right\}, \tag{33.16}$$

where $U(z)$ and W take complex form to reflect tidal phase variations. On substituting these into the momentum equation, we have

$$\mathrm{i}\omega U = -g\frac{\partial W}{\partial x} + N_z \frac{\partial^2 U}{\partial z^2}, \tag{33.17}$$

which has the solution

$$U = A_1 \mathrm{e}^{\mathrm{i}z/\delta} + A_2 \mathrm{e}^{-\mathrm{i}z/\delta} + C \tag{33.18}$$

with

$$\delta = \left(\frac{N_z}{\mathrm{i}\omega}\right)^{1/2} \tag{33.19}$$

and

$$C = -\frac{g}{\mathrm{i}\omega}\frac{\partial W}{\partial x}. \tag{33.20}$$

On applying boundary conditions, frictional stresses equal zero at the surface ($z = D$),

$$A_1 = A_2 \mathrm{e}^{-2D/\delta}, \tag{33.21}$$

and quadratic friction at the bed, $z = 0$, we have

$$\frac{8}{3\pi}k\left|\overline{U}\right|U_{z=0} = \frac{8}{3\pi}k\left|\overline{U}\right|(A_1 + A_2 + C), \tag{33.22}$$

where k is the friction coefficient and $|\overline{U}|$ is the depth-averaged velocity amplitude. With a total flow described as

$$\overline{U}D = \int_0^D U\,\mathrm{d}z = \delta A_1\left(\mathrm{e}^{D/\delta} - 1\right) - \delta A_2\left(\mathrm{e}^{-D/\delta} - 1\right) + CD, \tag{33.23}$$

which gives the following solution for U at any height z:

$$U(z) = \left(\frac{\mathrm{e}^{z/\delta} + \mathrm{e}^{-(z/\delta + y)}}{T} + Q\right)\overline{U}, \tag{33.24}$$

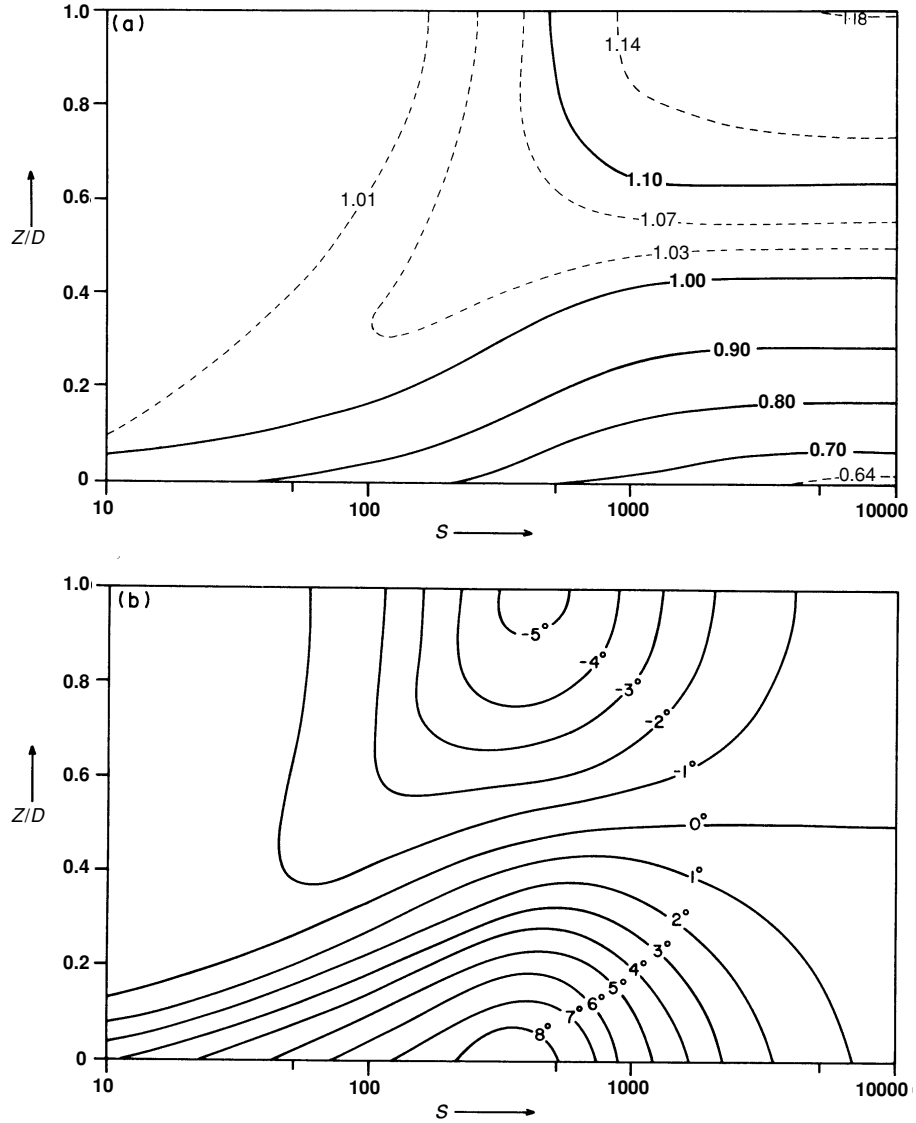

Fig. 33.1. The current profile as a function of the Strouhal number (with $k = 0.0025$ and $\alpha = 0.0012$). (a) The amplitude structure $|U(z)/\overline{U}|$; and (b) the phase structure $\theta(z) - \overline{\theta}$, taken from Prandle (1982a).

where

$$T = (1 - e^{2y})\left(j - \frac{1}{y} - 1\right) - 2e^{2y},$$

$$Q = \frac{j\left(1 - e^{2y}\right) - 1 - e^{2y}}{T}, \tag{33.25}$$

$$j = \frac{3\pi N_z}{8\delta k|\overline{U}|}$$

and

$$y = \frac{D}{\delta}, \tag{33.26}$$

so that the velocity profile is a function of the variables j and y. The modulus of y can be interpreted as a depth parameter converted to dimensionless form by Ekman scaling (Faller and Kaylor, 1969; Munk *et al.*, 1970; Prandle, 1982b). The modulus of j reflects the effect of the bottom stress through the bed stress coefficient k and the velocity $\overline{U}$.

By using the Bowden (1953) eddy-viscosity formulation $N_z = \alpha|\overline{U}|D$, the vertical structure of velocity is made only a function of a single parameter kS (McDowell, 1966), where S is the Strouhal number $S = 2\pi|\overline{U}|/(\omega D)$. Figure 33.1 shows the resultant velocity structure as a function of S with $k = 2.5 \times 10^{-3}$ and $\alpha = 1.2 \times 10^{-3}$ (Prandle, 1982a). For small values of S the current structure is uniform except for a small phase advance close to the bed. For larger values of S the variation in the current amplitude increases continuously, approaching an asymptote

in the region of $S = 1000$. It is also interesting to observe a midwater maximum in the region of $S = 100$. The phase variation also increases with increasing S, but it reaches a maximum difference between surface and bed in the region of $S = 350$; thereafter the variation decreases with increasing S with only 1° difference between bottom and bed for $S = 10\,000$.

Simpson *et al*. (2000) used a similar solution taken from Lamb (1932) to explain the phase lag of turbulence dissipation in a tidal flow. The solution used was

$$u(z) = C\frac{1-\cosh(1+\mathrm{i})(h-z)/\delta}{\cosh(1+\mathrm{i})h/\delta}\mathrm{e}^{\mathrm{i}\omega t}. \tag{33.27}$$

When $h/\delta \gg 1$ the solution near the bed is

$$u(z) = C\left(1-\mathrm{e}^{(1+\mathrm{i})z/\delta}\right)\mathrm{e}^{\mathrm{i}\omega t}. \tag{33.28}$$

As $z \to 0$, the velocity tends to

$$u(z) = C\sqrt{2}\frac{z}{\delta}\mathrm{e}^{\mathrm{i}(\omega t+\pi/4)}. \tag{33.29}$$

This means that the velocity near the bottom leads the free-stream velocity by $\pi/4$. The velocity shear is then given by

$$\frac{\partial u}{\partial z} = \mathrm{i}C\frac{\sqrt{2}}{\delta}\mathrm{e}^{-z/\delta}\mathrm{e}^{\mathrm{i}(\omega t-z/\delta+\pi/4)} \tag{33.30}$$

so that the phase lag of the shear relative to the forcing should increase with height above the bed as

$$\phi_2 = \frac{z}{\delta}+\frac{\pi}{4} = \left(\frac{\omega}{2N_z}\right)^{1/2}z+\frac{\pi}{4}, \tag{33.31}$$

so that

$$\frac{\partial u}{\partial z} = \mathrm{i}C\frac{\sqrt{2}}{\delta}\mathrm{e}^{-z/\delta}\cos(\omega t-\phi_2). \tag{33.32}$$

The corresponding production of turbulence kinetic energy (TKE) is

$$P = \rho N_z\left(\frac{\partial u}{\partial z}\right)^2 = -C^2\frac{\rho N_z}{\delta^2}\mathrm{e}^{-2z/\delta}\left[1+\cos\left(2\omega t-2\frac{z}{\delta}-\frac{\pi}{2}\right)\right]. \tag{33.33}$$

Therefore production, and hence dissipation, since we assume local equilibrium, will exhibit an M_4 variation in phase lag of

$$\phi_4 = 2\frac{z}{\delta}+\frac{\pi}{2} = \left(\frac{2\omega}{N_z}\right)^{1/2}z+\frac{\pi}{2}, \tag{33.34}$$

which increases with height at a rate that is twice that of the phase of the shear at the M_2 frequency. At the bottom boundary, the phase lag of production should be $\pi/2$, which is the same as the phase of the current speed near the bed.

A possible consequence of the phase delay in the production and dissipation of TKE may be manifested in the vertical diffusion of scalar properties upward from the seabed. In most turbulence-closure schemes the vertical diffusivity K_z increases with TKE intensity q, which is proportional to $\varepsilon^{1/3}$, so that the time of maximum K_z will also propagate up the water column. Under these conditions the scalar properties will pass up between layers as the diffusivity increases.

Evidence of the increasing phase delay with height in the periodic variation of concentrations of suspended particulate matter (SPM) at M_4 frequency has been observed in mixed waters of the Irish Sea (Campbell, 1996). The correlation between the M_4 phase for SPM and ε (Fig. 33.2) appears to favor the suggested mechanism.

33.1.5 Tidal-current boundary layers

It has long been recognized that tidal currents in shallow waters exhibit a marked variation in depth. In the first place, near-surface currents are generally stronger than near-bottom currents. Furthermore, the direction of maximum tidal streaming and its rotational properties might vary from surface to bottom. These observed vertical structures of tidal currents have successfully been explained by the use of theoretical models using arguments similar to those of Ekman or for oscillatory flows (Thorade, 1928; Prandle, 1982b; Soulsby, 1990). Examples of application of the theory to the planetary boundary layer and to oscillatory flow can be found in Prandle (1982b) and Soulsby (1983).

In studying first-order tidal propagation it is generally permissible to neglect vertical components of velocity and acceleration, convective terms, and density effects. The equations of motion along orthogonal axes x and y (east and north, respectively) may be written as (Bowden *et al*., 1959)

$$\frac{\partial u}{\partial t}-fv = -g\frac{\partial \zeta}{\partial x}+\frac{1}{\rho}\frac{\partial}{\partial z}F_{zx}, \tag{33.35}$$

$$\frac{\partial v}{\partial t}+fu = -g\frac{\partial \zeta}{\partial y}+\frac{1}{\rho}\frac{\partial}{\partial z}F_{zy}, \tag{33.36}$$

where z is the vertical coordinate positive upward from the bottom; u and v are the x and y velocities, respectively; f is the Coriolis parameter, g is the gravitational acceleration; ζ is the surface elevation, and ρ is the density.

Consider a single tidal harmonic of frequency ω. The velocity components can be written

$$V = a_v\cos(\omega t)+b_v\sin(\omega t), \tag{33.37}$$

$$U = a_u\cos(\omega t)+b_u\sin(\omega t), \tag{33.38}$$

where U and V vary sinusoidally with time with different amplitudes and phases. The combination of U and V defines a current vector, which rotates about a fixed origin and describes an elliptical path. To investigate the structure of the tidal currents, it is advantageous to divide the ellipse into the sum of two circular motions, one rotating clockwise (R_-) and the other anti-clockwise (R_+) (Thorade, 1928; Godin, 1972; Souza and Simpson, 1996a).

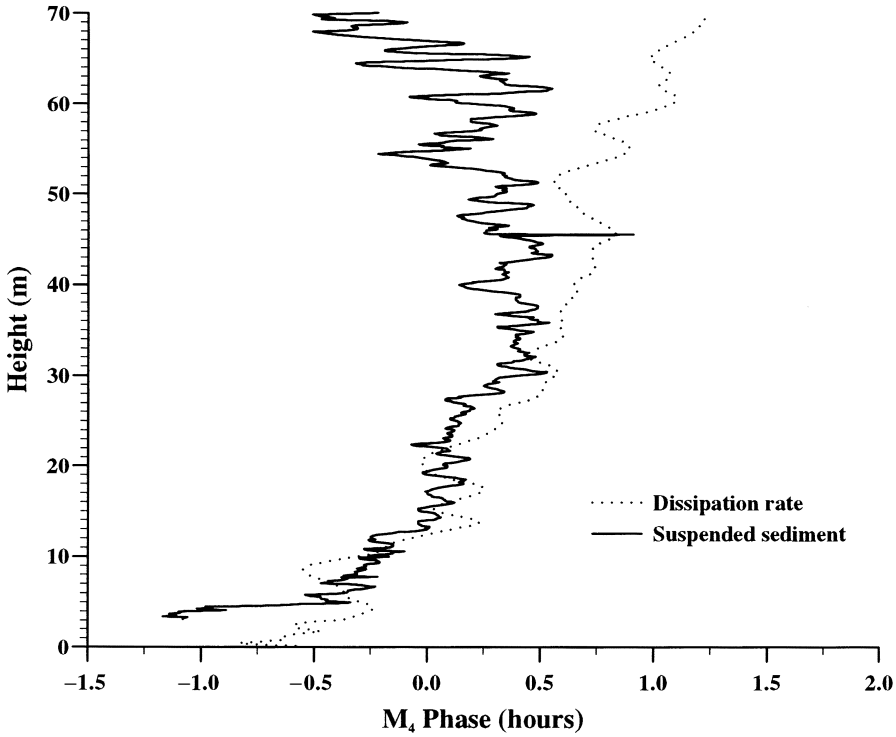

Fig. 33.2. Phases for SPM (continuous line) and ε (dotted) in a mixed site of the Irish Sea, from Campbell (1996).

This can readily be achieved by introducing complex vector notation with x being the real and y the complex axis. The velocity vector, R, is given by

$$R = U + \mathrm{i}V \tag{33.39}$$

so that

$$R = R_+ + R_- \tag{33.40}$$

with

$$R_+ = [a_u + b_v + \mathrm{i}(a_\mathrm{b} - b_\mathrm{b})]\mathrm{e}^{\mathrm{i}\omega t} \tag{33.41}$$

and

$$R_- = [a_u - b_v + \mathrm{i}(a_\mathrm{b} + b_\mathrm{b})]\mathrm{e}^{-\mathrm{i}\omega t}. \tag{33.42}$$

Using this transformation, the equations of motion are

$$\begin{aligned} \mathrm{i}(f+\omega)R_+ &= S_+ + N_z \frac{\partial^2 R_+}{\partial z^2} \qquad \text{(anti-clockwise)}, \\ \mathrm{i}(f-\omega)R_- &= S_- + N_z \frac{\partial^2 R_-}{\partial z^2} \qquad \text{(clockwise)} \end{aligned} \tag{33.43}$$

with boundary conditions

$$N_z \frac{\partial R_\pm}{\partial z} = \begin{cases} 0, & \text{at } z = 0 \\ k_\mathrm{b} R_\pm, & \text{else.} \end{cases} \tag{33.44}$$

The equations are mathematically identical to those for the oscillating boundary layer and could be solved immediately by substituting δ for $\delta_\pm$, where

$$\delta_\pm = \left(\frac{N_z}{\mathrm{i}(f \pm \omega)} \right)^{1/2} \tag{33.45}$$

with an effective boundary-layer thickness (Soulsby, 1983) given by

$$\delta = \frac{R_+\delta_+ + R_-\delta_-}{R_+ + R_-}. \tag{33.46}$$

Alternatively, because the equations are also identical to Ekman's, we can borrow his solution, following Maas and van Haren (1987).

This solution explains the general behavior of the tidal currents (Soulsby, 1983, 1990; Prandle, 1982a,1982b; Maas and van Haren, 1987), but there are exceptions related to the effect of stratification over the distribution of the eddy viscosity N_z (Maas and van Haren, 1987; Lwiza *et al.*, 1992; Souza and Simpson, 1996a). In Fig. 33.3 we can observe how the change in stratification, represented by the bulk Richardson number, appears to be related to the vertical change of ellipticity in the Rhine and Liverpool Bay regions of freshwater influence. This can be explained by a discontinuity in the eddy viscosity due to the stratification. An extension of the above model including this change in N_z can be found in Visser *et al.* (1994). More advanced numerical models using Mellor and Yamada (1974) closure

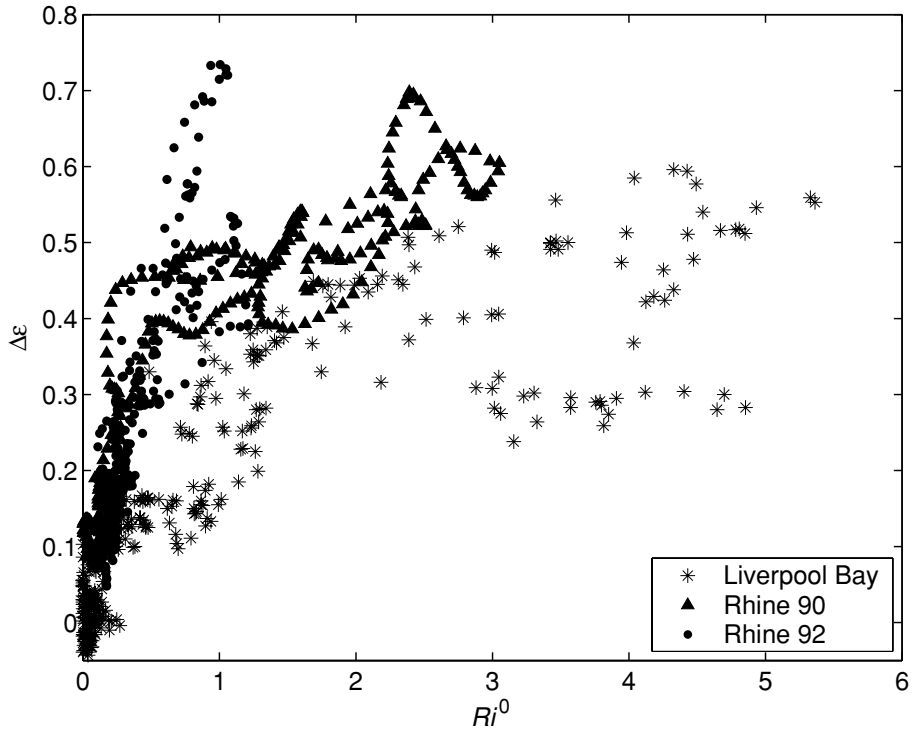

Fig. 33.3. The relationship between the bottom-surface ellipticity difference and the bulk Richardson number for Liverpool Bay (asterisk) and the Rhine ROFI (triangle and dots).

schemes have successfully reproduced this effect (Souza and Simpson, 1996b).

33.2 Wave–current interaction

33.2.1 Introduction

The wave and current field interact mutually through a number of mechanisms: modification of kinematics due to sheared currents; generation by waves of mass transport or streaming currents; enhancement of the bottom friction felt by the currents, due to interaction with the wave boundary layer; and enhancement of the bed shear stress and energy dissipation of the waves, due to interaction with the current boundary layer. This modification of the bed shear stress appears to be important in determining the distribution of SPM.

The orbital motions produced by waves decrease with increasing depth beneath the surface. However, in water whose depth is less than $0.16gT_w^2$ (T_w is the wave period), appreciable orbital velocities reach the seabed, where they produce an oscillatory bed shear stress. If waves are superimposed on a current, the wave and current boundary layers interact in such a way that the time-mean bed shear stress is larger than that for the same depth-averaged current in the absence of waves. This is equivalent to increasing the mean drag coefficient for a given physical roughness of the seabed. Thus, for a given amplitude of slope of a tidal oscillatory water surface, the amplitude of the tidal current velocity will be smaller when waves are present than when they are not. This behavior applies particularly to shallow water, partly because the tidal currents are less dependent on friction in deep water, and partly because the wave orbital velocities do not penetrate to the bed in deep water (Soulsby, 1990).

Most of the models of the wave–current bottom boundary and derived bed shear stress follow the work of Grant and Madsen (1979). In this work we will explain the problem of coupling hydrodynamic models with models of the bottom boundary layer that include wave–current interaction and discuss how has this been approached by several authors.

33.2.2 Implementation of wave–current interaction in hydrodynamic models

A recent problem that has been a focus of attention for numerical modelers is the coupling of hydrodynamic models with models of the bottom boundary layer that include wave–current interaction (Keen and Glenn, 1994; Davies and Lawrence, 1994a; Lou and Ridd, 1997). In these models, the effect that interaction with sediment has on the flow (Glenn and Grant, 1987) is generally discarded, as in the case of Keen and Glenn (1994). One of the most common approaches is that used by Signell *et al*. (1990). For

simplicity we will concentrate on collinear flow, although the extension to waves and currents at an arbitrary angle is not complicated (Grant and Madsen, 1979). Hence, the total bed shear stress τ_T based upon the instantaneous current stress τ_c and maximum wave bed stress τ_w is given by

$$\tau_T = \tau_c + \tau_w \tag{33.47}$$

with

$$\tau_w = \tfrac{1}{2} f_w \rho U_o^2, \tag{33.48}$$

where U_o is the maximum near-bed wave orbital velocity and f_w is the wave friction factor.

The near-bed orbital velocity is given by

$$U_o = \frac{a_w \omega}{\sinh(kh)} \tag{33.49}$$

with a_w as the wave amplitude, ω the wave frequency, and k the wavenumber given by the linear dispersion relation

$$\omega^2 = gk \tanh(kh). \tag{33.50}$$

The wave friction factor f_w is obtained using the empirical expressions from Grant and Madsen (1982), which represent the best fit to data:

$$f_w = \begin{cases} 0.13(k_b/A_b)^{0.40}, & \text{for } k_b/A_b < 0.08, \\ 0.23(k_b/A_b)^{0.62}, & \text{for } 0.08 < k_b/A_b < 1.0, \\ 0.23, & \text{for } k_b/A_b > 1.0, \end{cases} \tag{33.51}$$

where $k_b = 30 z_0$, where z_0 is the roughness length, and $A_b = U_o/\omega$.

The effective drag coefficient f_c taking into account wave effects and assuming that the current does not influence the wave field is calculated following Davies and Lawrence (1994a). The wave friction velocity is given by

$$U_{*w} = \left(\frac{\tau_w}{\rho}\right)^{1/2}. \tag{33.52}$$

The initial condition for the current factor excluding wind-wave turbulence was determined from

$$f_c = 2\left(\frac{\kappa}{\ln(30 z_r/k_{bc})}\right)^2, \tag{33.53}$$

where κ is von Kármán's constant, $k_{bc} = k_b$, for this initial calculation, and z_r is the reference height at which the slip condition is applied.

Once f_c has been calculated, U_{*c} can be computed from

$$U_{*c} = \left(\frac{\tau_c}{\rho}\right)^{1/2}. \tag{33.54}$$

The combined friction velocity U_{*cw} for waves and currents is given by

$$U_{*cw} = \left(U_{*c}^2 + U_{*w}^2\right)^{1/2}. \tag{33.55}$$

The apparent bottom roughness k_{bc} felt by the current due to the presence of a wave is given by

$$k_{bc} = k_b \left(C_1 \frac{U_{*cw}}{U_w} \frac{A_b}{k_b}\right)^{\beta} \tag{33.56}$$

with $C_1 = 24.0$ (Grant and Madsen, 1979) and

$$\beta = 1 - \frac{U_{*c}}{U_{*cw}}. \tag{33.57}$$

This value of k_{bc} is then used at the next time step to determine f_c and hence the bed stress. Similar approaches have been followed by other authors (e.g. Davies and Lawrence, 1994b; Lou and Ridd, 1997), but using the wave friction factor f_w as defined by Jonsson and Carlsen (1976), namely

$$\frac{1}{4\sqrt{f_w}} + \log_{10}\left(\frac{1}{4\sqrt{f_w}}\right) = -0.08 + \log_{10}\left(\frac{A_b}{k_b}\right). \tag{33.58}$$

In most of the works the authors tend to calculate the bottom stress by using the combined wave–current drag coefficient to derive U_{*c} (e.g. Davies and Lawrence, 1994b; Signell and List, 1997). However, recent work by Souza *et al.* (2001) suggested the need to use the full combined bottom stress in order to be able to account for the levels of mixing and resuspenison of particulate matter under hurricane waves.

Comparisons between field data from various areas in the North Sea and a similar combined wave–current stress (Christoffersen and Jonsson, 1985) show qualitative agreement, although there is a tendency to overestimate the stress under low-wave conditions and underestimate it under high-wave conditions (Wolf, 1999).

33.2.3 Generalized wave–current bottom stress

Although the Grant and Madsen (1979) formulation is probably the most commonly used in the literature, this obviously does not mean that is the only one, as there are more than 20 models describing the combined wave–current boundary layer (Soulsby *et al.*, 1993). Soulsby *et al.* (1993) also mentioned that, for sediment-transport purposes, it is important to calculate the time-mean bed shear stress τ_m and the maximum bed shear stress τ_{max}, in the wave–current flow. The threshold of motion and entrainment of sediment are determined by τ_{max}, whereas the current velocity and diffusion of SPM into the upper part of the flow are determined by τ_m.

Soulsby *et al.* (1993) tried to formulate a generalized parameterization for all the models. Their approach was based on first of all calculating the friction factors f_c and f_w independently assuming that there are no interactions, so that

$$f_c = \left(\frac{\kappa}{\ln(z_r/z_0)}\right)^2 \tag{33.59}$$

and

$$f_w = 1.39\left(\frac{A_b}{z_0}\right)^{-0.52} \tag{33.60}$$

and then calculating τ_{max} and τ_m as

$$\tau_{max} = Y(\tau_c + \tau_w) \tag{33.61}$$

and

$$\tau_m = y(\tau_c + \tau_w) \tag{33.62}$$

with

$$Y = 1 + ax^m(1-x)^n, \tag{33.63}$$

and

$$y = x[1 + bx^p(1-x)^q], \tag{33.64}$$

and

$$x = \frac{\tau_c}{\tau_c + \tau_w}, \tag{33.65}$$

where

$$a = (a_1 + a_2|\cos\phi|^I) + (a_3 + a_4|\cos\phi|^I)\log_{10}(f_w/f_c) \tag{33.66}$$

with analogous expressions for m and n, and

$$b = (b_1 + b_2|\cos\phi|^J) + (b_3 + b_4|\cos\phi|^J)\log_{10}(f_w/f_c) \tag{33.67}$$

with analogous expressions for p and q, and the coefficients chosen from Table 33.1 for six different models.

The wave–current non-linear interactions are expressed in the Y and y parameters. For example, in the case with non-linear interactions $\tau_m = \tau_c$; hence $y = x$. A comparison of the parameterized expression with direct-model results from Fredsøe (1984) is shown in Fig. 33.4 for a range of angles ϕ. There is reasonably good agreement.

This parameterization appears to be simple to implement as a bottom boundary condition in any hydrodynamic model. It has the advantage that any of the six models tested can be readily applied merely by changing the appropriate coefficients.

33.2.4 Production of TKE due to waves

A better approach to parameterization of the wave–current interaction was recently developed by Mellor (2002). This approach, instead of using the modified bed stress as a boundary condition, uses the production of TKE generated by waves directly in the turbulence-closure formulation. The effect of waves on the mean current flow is felt through an increase of N_z due to an increase of TKE (q^2), which is the result of an increase in shear production. Hence, following Mellor (2002), the shear-production equation is

$$P_s = N_z\left[\left(\frac{\partial u}{\partial z}\right)^2 + \left(\frac{\partial v}{\partial z}\right)^2\right] + P_w, \tag{33.68}$$

where P_w is the apparent shear production due to waves,

$$\left(\frac{P_w}{\omega A^2}\right)^{1/3} = F_\phi\left(\phi, \frac{u_*}{A}\right)F_z\left(\frac{z\omega}{A}, \frac{z_0\omega}{A}\right). \tag{33.69}$$

F_z was obtained diagnostically from the shear production in purely oscillatory cases for various values of z_0 by curve fitting. This gave

$$\begin{aligned} F_z = {} & -0.0465 + 0.027\,78\ln\left(\frac{z\omega}{A}\right) + 0.016\,22\left[\ln\left(\frac{z\omega}{A}\right)\right]^2 \\ & - \log_{10}\left(\frac{z_0\omega}{A}\right)\left\{-0.102 - 0.002\,53\ln\left(\frac{z\omega}{A}\right)\right. \\ & \left. + 0.002\,73\left[\ln\left(\frac{z\omega}{A}\right)\right]^2\right\} \end{aligned} \tag{33.70}$$

and

$$F_\phi = 1.22 + 0.22\cos(2\phi). \tag{33.71}$$

Before applying this formulation, we should modify the law of the wall to account for the added shear production, so the logarithmic layer, instead of being like in Section 33.1, will be defined as

$$U = \frac{u_*^2}{\kappa S_{M0} q_0}\ln\left(\frac{z_r}{z_0}\right). \tag{33.72}$$

This is a general formulation of the logarithmic layer, which includes the standard situation of $P_w = 0$, so that $S_{M0}q_0 = u_*$. A comparison of the use of this parameterization with resolved simulations is shown is Fig. 33.5.

33.3 Effects of sediment

33.3.1 Introduction

Sediment affects hydrodynamics and turbulence within the bottom boundary layer in three fundamental ways: by forming bottom roughness, damping turbulence, and creating a down-slope pressure gradient. Needless to say, suspended sediment concentrations and bedforms are, in turn, strong functions of boundary-layer hydrodynamics. However, the focus here is mainly on how sediments affect the flow such that hydrodynamic models may need to consider their presence in order to provide accurate predictions. For aspects of sediment transport as a response to hydrodynamics (i.e. without large effects on the flow itself), the reader is referred to such works as Dyer (1986), Nielsen (1992), and van Rijn (1992).

33.3.2 Bottom roughness

Sediment-related features typically make a dominant contribution to bottom roughness, although effective roughness can also be modified or dominated by biological activities. For steady homogeneous flow within the logarithmic layer, a key parameter is the hydraulic roughness, z_0 (see Eq. (33.3)), which has been shown in the laboratory

Table 33.1. Fitting coefficients for various models[a]

	a_1	a_2	a_3	a_4	m_1	m_2	m_3	m_4	n_1
F84	—	1.70	—	0.29	0.67	—	0.09	0.42	0.75
	0.06		0.29			0.29			
MS90	—	1.84	—	−0.22	0.63	—	0.23	–0.02	0.82
	0.01		0.58			0.09			
HT91	—	1.87	—	–0.12	0.72	—	0.08	0.34	0.78
	0.07		0.34			0.33			
GM79	0.11	1.95	—	0.28	0.65	—	0.15	0.06	0.71
			0.49			0.22			
DSK88	0.05	1.62	—	0.25	1.05	—	—	0.59	0.66
			0.38			0.72	0.08		
B67	0.00	2.00	0.00	0.00	0.00	0.50	0.00	0.00	0.00

	n_2	n_3	n_4	I	b_1	b_2	b_3	b_4	p_1
F84	—	0.11	—	0.80	0.29	0.55	—	−0.14	—
	0.27		0.02				0.10		0.77
MS90	—	0.19	—	0.67	0.65	0.29	—	−0.21	—
	0.30		0.21				0.30		0.60
HT91	—	0.12	—	0.82	0.27	0.51	—	−0.24	—
	0.23		0.12				0.10		0.75
GM79	—	0.17	—	(0.67)	0.73	0.40	—	−0.24	—
	0.19		0.15				0.23		0.68
DSK88	—	0.19	—	(0.82)	0.22	0.73	—	−0.35	—
	0.25		0.03				0.05		0.86
B67	0.50	0.00	0.00	(0.80)	0.32	0.55	0.00	0.00	—
									0.63

	p_2	p_3	p_4	q_1	q_2	q_3	q_4	J
F84	0.10	0.27	0.14	0.91	0.25	0.50	0.45	3.0
MS90	0.10	0.27	—	1.19	—	0.22	—	0.50
			0.06		0.68		0.21	
HT91	0.13	0.12	0.02	0.89	0.40	0.50	0.28	2.7
							—	
GM79	0.13	0.24	—	1.04	—	0.34	—	(0.50)
			0.07		0.56		0.27	
DSK88	0.26	0.34	—	−0.89	2.33	2.60	—	(2.7)
			0.07				2.50	
B67	0.05	0.00	0.00	1.14	0.18	0.00	0.00	(3.0)

[a] F84, Fredsøe (1984); MS90, Myrhaug and Slaatelid (1990); HT91, Huynh-Thanh and Temperville (1991); GM79, Grant and Madsen (1979); DSK88, Davies *et al*. (1988); and B67, Bijker (1967). Bracketed values of I and J are obtained indirectly, by analogy with other models.

to be equal to between $D/15$ and $D/30$ for a flat bed composed of stationary sand grains of diameter D (e.g. Dyer, 1986). In the field, sedimentary bedforms of various wavelengths often cause z_0 to be much larger, typically of the order of η^2/λ, where η is the bedform height and λ is the bedform length (Grant and Madsen, 1982). For steady flow over sand, a hierarchy of bedforms is often present, with ripples ($\lambda \approx 30$ cm) superimposed on dunes ($\lambda \approx 10$ m), superimposed on large sandwaves ($\lambda \approx 100$ m) (Soulsby, 1983). A nested series of logarithmic layers can result, with sand-grain roughness determining z_0 nearest the bed, but larger z_0 values due to bedforms resulting from log-linear fits to observed velocity further from the bed. The shear velocity, u_*, associated with the nested logarithmic profiles likewise increases with distance from the bed as form drag is added to skin friction.

The physics of sandy-bedform equilibria even under steady flow is highly non-linear and beyond the scope

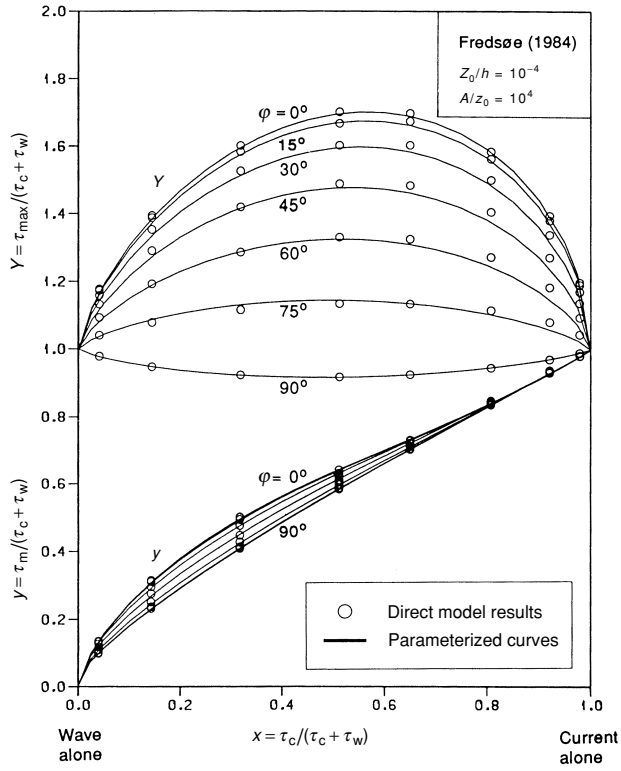

Fig. 33.4. A comparison of fitted curves with directly computed results from the model of Fredsøe (1984), for a range of angles in 15° increments, from Soulsby *et al.* (1993).

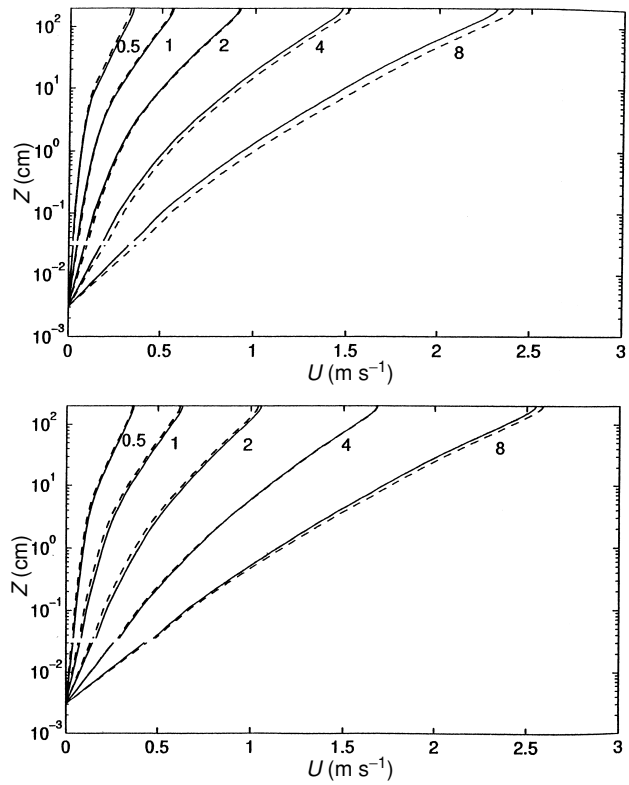

Fig. 33.5. A comparison of phase-averaged resolved solutions (solid curves) with the parameterized solutions (dashed curves) using Eqs. (33.21)–(33.24). The labels on the curves are $\overline{\tau}_{0x}$, with units of $10^{-3}\,\mathrm{m^2\,s^2}$. The oscillatory parameters are $\omega = 9.6\,\mathrm{s^{-1}}$ and $z_0 = 3.06 \times 10^{-5}$. (a) $(A_x, A_y) = (2, 0)\ \mathrm{m\,s^{-1}}$ so that $\phi = 0°$. (b) $(A_x, A_y) = (0, 2)\ \mathrm{m\,s^{-1}}$ so that $\phi = 90°$, from Mellor (2002).

of this review. Qualitatively, the general progression with increasing bed stress is from ripples to dunes, to plane bed, to antidunes. However, it should be kept in mind that physical bedforms are not always in equilibrium with overlying flow, particularly when energy is decreasing. An empirical summary of moderate-sized bedform types as a function of sand-grain size and steady flow velocity is provided by Southard and Boguchwal (1990). For sand under waves, a somewhat similar progression of bedforms is seen with increasing energy, from regular ripples, to cross-ripples, to megaripples, to plane bed (Clifton, 1976). An empirical summary of ripple geometry as a function of sand-grain size, wave period, and wave amplitude is provided by Wiberg and Harris (1994). The transition to megaripples is discussed by Vincent *et al.* (1999).

Over cohesive beds subjected to steady currents, physical bedforms affecting the hydrodynamics of the bottom boundary layer generally run parallel to the flow rather than perpendicular (e.g. Dellapenna *et al.*, 2001; Whitehouse *et al.*, 2000). These bedforms (termed ridges, runnels, or furrows) commonly occur in moderately energetic, quasi-steady flow environments and typically exhibit vertical relief of a few tens of centimeters, widths $O(1\,\mathrm{m})$, and spacing $O(1\text{–}10\,\mathrm{m})$. The physics of muddy bedforms is even less well understood than that of their sandy counterparts. In the absence of physical bedforms, the roughness of moderately energetic muddy bottoms is typically dominated by sedimentary structures formed by biological activity. Even though the sedimentary structures are not physically formed, it still may be reasonable to approximate z_0 as η^2/λ, where η and λ represent the characteristic height and spacing of the biologically modified roughness elements (Harris and Wiberg, 1997).

As the intensity of sediment transport increases, the presence of mobile sediment near the bed also affects the bottom roughness felt by the overlying flow. For steady sheet flow of sand over a plane bed, Sumer *et al.* (1996) showed that z_0 increases with the dimensionless bed stress (the Shields parameter) for cases with sand-settling velocity, w_s, greater than u_*. For sheet flow with $w_s < u_*$, z_0 was shown to be a function both of the Shields parameter and of w_s/u_* (the Rouse parameter). Sheet flow roughness under waves is thought to be similar to that under steady flow, albeit responding more or less instantaneously to the time-varying fluid velocity at the top of the sheet

layer (Dohmen-Janssen and Hanes, 2002). The effect of mud on bottom roughness under intense sediment transport is very different and less well studied. For steady flow in fluid mud, concentrations can be so high that shear is controlled by non-Newtonian fluid viscosity, and z_0 is no longer a relevant parameter (Vinzon and Mehta, 2001). Under intense oscillatory flow, mud bed can become a viscoelastic continuum with the overlying water column, such that wave motion occurs well into the "bed" (Jiang and Mehta, 1996). Wave-energy attenuation is then much greater than would be predicted from a standard estimate of bottom roughness.

33.3.3 Damping of turbulence

Suspended sediment is a source of stabilizing buoyancy within the bottom boundary layer and thus affects turbulence and shear in a manner analogous in many ways to thermohaline stratification. For example, Gross and Dade (1991) demonstrated that moderate concentrations of fine sediment can reduce the thickness of the planetary bottom boundary layer. Trowbridge and Kineke (1994) showed that damping of turbulence by sediment-induced stratification can drastically alter velocity profiles within an oscillatory momentum-deficit layer. Winterwerp (2001) recently applied a one-dimensional k-ε model to examine modifications to velocity and turbulence in open-channel flow due to suspended sediment. Several authors have specifically focused on the modification sediment-induced stratification makes to shear within the logarithmic or, in the context of stratified flow, more appropriately termed "overlap" layer, where aspects of inner and outer boundary-layer scalings simultaneously apply (e.g. Smith and McLean, 1977; Glenn and Grant, 1987; Villaret and Trowbridge, 1991).

Consideration of turbulent buoyancy flux due to suspended sediment, $b_f = gs\langle C'w'\rangle$, introduces the stability parameter, ζ, to dimensionless scaling of the overlap layer (Kundu, 1990):

$$\frac{\mathrm{du}}{\mathrm{dz}} = \frac{u_*}{\kappa z}(1 + \alpha\zeta), \tag{33.73}$$

where $\zeta = (b_f \kappa z)/u_*^3$, $\kappa \approx 0.4$ is von Kármán's constant, $s \approx 1.7$ is the submerged weight of sediment relative to water, C is the volume concentration of suspended sediment, w is the vertical velocity, and $\alpha \approx 5$ is an additional empirical constant. The form of (33.73) is justified by a truncated Taylor expansion in ζ, although (33.73) is commonly assumed to be exact when applied to sediment-induced stratification in the overlap layer (Smith and McLean, 1977; Glenn and Grant, 1987; McLean, 1992). In a weakly stratified overlap layer, the variation of ζ with z is monotonically similar to both that of the gradient Richardson number, Ri (Friedrichs *et al.*, 2000), and to that of the flux Richardson number, Ri_f (Villaret and Trowbridge, 1991). In general, the presence of suspended sediment causes ζ to be positive, and (33.73) indicates that the slope of the observed logarithmic profile will then overestimate u_*.

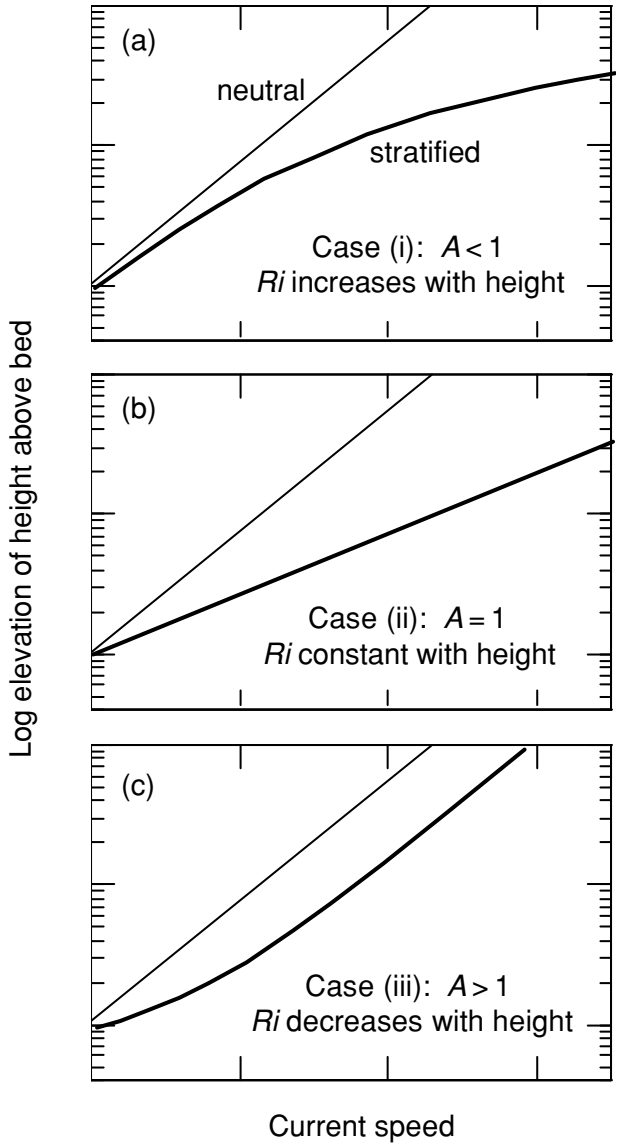

Fig. 33.6. Idealized velocity profiles corresponding to three cases of sediment-induced stratification with $C \sim z^{-A}$: (a) $A < 1$, (b) $A = 1$, and (c) $A > 1$. Thin line, neutral profile; thick line, stratified profile. Modified from Friedrichs *et al.* (2000).

In examining (33.73), Friedrichs *et al.* (2000) demonstrated how the shapes of the concentration and velocity profiles are coupled within the overlap layer for cases in which the sediment concentration profile approximates a power law $C \sim z^{-A}$ (Fig. 33.6): (i) if $A < 1$, it can be shown that ζ and Ri both increase with z, and it follows from (33.73) that a log-linear representation of (33.73) will be concave downward; (ii) if $A = 1$, then ζ and Ri are constant in z, and u will remain logarithmic; and (iii) if $A > 1$, then ζ and Ri decrease with increasing z and a log-linear

velocity curve is concave upward. As z increases in case (i), stabilizing stratification becomes more important relative to destabilizing shear and more shear (relative to a logarithmic profile) is necessary to support a given level of stress. As z increases in case (iii), stratification becomes less important and less shear (relative to case (i)) is needed to support a given level of stress. Since A is close to the Rouse parameter for moderately low concentrations (Glenn and Grant, 1987), moderately intense suspensions of fine sediment will tend to exhibit concave-downward deviations from a logarithmic profile and an anomalous decrease in turbulence away from the bed, whereas moderately intense suspensions of coarse sediment will tend to exhibit concave-upward deviations and an anomalous decrease in turbulence toward the bed.

Suspended sediment can ultimately provide so much stabilizing buoyancy that it shuts down the generation of turbulence by shear. One simple scaling for this critical "saturation concentration," $C_{\rm cr}$, is to solve for the sediment concentration at which the flux Richardson number exceeds the critical value possible for shear-generated turbulence, $Ri_{\rm fcr} \approx \frac{1}{5}$. Winterwerp (2001) did this by assuming unstratified logarithmic layer scaling for the components of $Ri_{\rm fcr}$, which yields

$$C_{\rm cr} = Ri_{\rm fcr} u_*^3/(gsw_{\rm s}\kappa z). \tag{33.74}$$

An analogous concept can be applied to the entire bottom boundary layer by assuming that shear generation is governed by a critical gradient Richardson number. Wright *et al.* (2001) argued that, in a bottom boundary layer critically stratified by fine sediment, $Ri_{\rm cr} = B/U_{\rm max}^2 \approx \frac{1}{4}$, where B is the depth-integrated buoyancy anomaly and $U_{\rm max}$ is the amplitude of the dominant (wave or current) velocity at the top of the boundary layer. The critically stratified, depth-integrated sediment load is then

$$L_{\rm cr} = \rho_{\rm s} U_{\rm max}^2 Ri_{\rm cr}/(gs), \tag{33.75}$$

where $\rho_{\rm s} \approx 2700\ {\rm kg\,m^{-3}}$ is a typical inorganic sediment density.

Under energetic conditions with abundant, easily suspended sediment, (33.74) and (33.75) represent stable equilibria (Wright *et al.*, 2001) because additional shear will reduce the Richardson number below its critical value, markedly increasing turbulence and suspending more sediment until the Richardson number becomes critical once more. Conversely, a reduction in shear will increase the Richardson number above $Ri_{\rm cr}$, markedly decreasing turbulence and depositing sediment until Ri once more returns to critical. If shear decreases too rapidly, however, a catastrophic collapse of turbulence throughout the boundary layer is possible since hindered settling prevents complete deposition onto the bed (Winterwerp, 2001).

Consideration of simplified momentum and sediment-transport equations allows analytical prediction

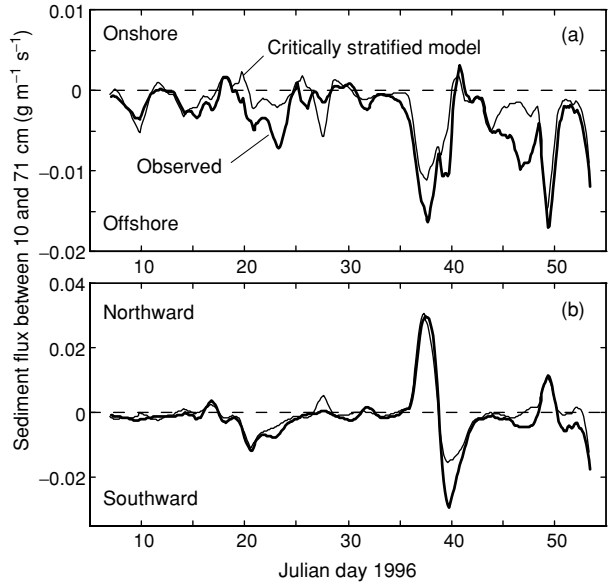

Fig. 33.7. A comparison of observed sediment flux with predictions obtained by using a critically stratified model for the northern California shelf (observations from Wright *et al.* [1999]). The inputs to the model are $\alpha = 1/Ri_{\rm cr} = 4$ and $u_*^2/w_{\rm s}$ based on observed velocity between 10 and 71 cm above the bed. Observations and model predictions are passed through a 24-h running mean. Thin line, critically stratified model; thick line, observations.

of the eddy viscosity and velocity profiles within critically stratified boundary layers. By assuming that $\alpha\zeta \gg 1$ in (33.73) (requiring $w_{\rm s}/u_* \ll 1$), equating eddy viscosity and diffusivity, and applying a balance between upward turbulent diffusion of sediment and gravitational settling, it follows that, within the overlap layer (Fig. 33.7),

$$A_{z{\rm cr}} = w_{\rm s} z, \tag{33.76}$$

$$u_{\rm cr} = (u_*^2/w_{\rm s}) \log_{10}(z/z_0), \tag{33.77}$$

$$C_{\rm cr} = (u_*^2/w_{\rm s})^2 (\alpha g s z)^{-1}. \tag{33.78}$$

From (33.76)–(33.78) it also follows that $\alpha = 1/Ri_{\rm cr}$. The solution for $C_{\rm cr}$ in (33.78) differs from (33.74) by a factor of $u_*/(\kappa w_{\rm s})$ because (33.76)–(33.78) involve solving explicitly for ${\rm d}u_{\rm cr}/{\rm d}z$ rather than approximating ${\rm d}u/{\rm d}z$ using the unstratified logarithmic-layer value.

Trowbridge and Kineke (1994) provided similarity solutions for the momentum-deficit layer that also satisfy simplified momentum and sediment-transport relations and assume that $Ri_{\rm f} = Ri = Ri_{\rm cr}$. Assuming that $w_{\rm s}/u_* \ll 1$ and that there is a small velocity at the top of the underlying wall layer, their solutions reduce to

$$A_z = (\delta/2)(u_*^2/U_{\rm max})[(z/\delta)^{-1} - (z/\delta)^2], \tag{33.79}$$

$$u_{\rm cr} = U_{\rm max}(z/\delta)^2, \tag{33.80}$$

$$C_{\rm cr} = \tfrac{4}{3} U_{\rm max}^2 Ri_{\rm cr} (\delta g s)^{-1} [1 - (z/\delta)^3], \tag{33.81}$$

where δ is the thickness of the boundary layer. If integrated over the bottom boundary, (33.81) becomes exactly equivalent to (33.74). Trowbridge and Kineke's solution for A_z becomes unrealistically large as one approaches the bed. They suggest matching A_z to the overlap-layer solution at the height at which turbulence-energy production, $P = A_z(\mathrm{d}u/\mathrm{d}z)^2$, predicted in the overlap layer exceeds that predicted by (33.79)–(33.81).

33.3.4 Downslope pressure gradients

Like salt and heat, suspended sediment can also create horizontal pressure gradients that drive significant currents. We consider here only sediment-induced gravity currents initially suspended by hydrodynamic processes. Relevant examples include self-accelerating gravity currents initially formed by wave resuspension of sand on the shoreface (Seymour, 1986), muddy gravity currents suspended near shore by strong currents near river mouths, but which decay offshore (Wright *et al.*, 1990), and equilibrium muddy gravity currents on the shelf suspended by waves or currents (Traykovski *et al.*, 2000). For a recent review of sediment gravity currents of other types (e.g. slope failures, debris flows), see Parsons *et al.* (2004).

If the seabed slopes downward in the x direction at an angle β, then suspended sediment produces a down-slope pressure gradient capable of driving a down-slope contribution to velocity, u_g, governed by the following quasi-steady momentum balance:

$$Csg \sin\beta = \frac{\mathrm{d}}{\mathrm{d}z} A_z \frac{\mathrm{d}u_g}{\mathrm{d}z}. \tag{33.82}$$

Equation (33.82) integrates over the bottom boundary layer to approximately (Wright *et al.*, 2001)

$$B \sin\beta = c_\mathrm{d} U_g U_\mathrm{max} \tag{33.83}$$

where U_g is the strength of the gravity current near the top of the boundary layer, and c_d is a bottom drag coefficient. Equation (33.83) employs a linearized quadratic drag formulation, which recognizes that shear associated with u_g is not necessarily the dominant source of turbulence contributing to A_z.

Combining (33.75) with (33.83) to eliminate B yields the maximum down-slope velocity for a turbulent gravity flow initiated by hydrodynamic suspension (Wright *et al.*, 2001):

$$U_{g\mathrm{cr}} = (\sin\beta) Ri_\mathrm{cr} U_\mathrm{max}/c_\mathrm{d}. \tag{33.84}$$

On the basis of (33.84), fluid mud in an energetic tidal boundary layer ($U_\mathrm{max} = 1\ \mathrm{m\,s^{-1}}$) with $c_\mathrm{d} = 0.003$ is predicted to move down a relatively mild 1/200 slope at a remarkable 40 $\mathrm{cm\,s^{-1}}$ (c.f. Kineke *et al.*, 1996). Equation (33.84) is an upper limit on U_gcr because it assumes high concentrations throughout the boundary layer ($w_\mathrm{s}/u_* \ll 1$). Nonetheless, currents predicted by (33.84) have been shown to be consistent with mud-laden wave boundary layers on the northern California shelf (Scully *et al.*, 2002). Ongoing research (by C. T. Friedrichs) is investigating the role of finite settling velocity in determining the speed of such gravity flows.

For the case in which U_g is of the same order as ambient waves or currents (i.e. $U_\mathrm{max} = U_g$), employing the approximation $Ri = B/U_\mathrm{max}^2$ gives (Wright *et al.*, 2001)

$$Ri = c_\mathrm{d}/\sin\beta. \tag{33.85}$$

Assuming that c_d is about 0.003–0.005 (Wright *et al.*, 2001) and that $Ri_\mathrm{cr} = \frac{1}{4}$, suspensions over slopes greater than about 0.02 have the potential of self-accelerating due to additional suspension from the bed by stress associated with the gravity current itself (c.f. Parker *et al.*, 1986). This explains why self-accelerating gravity currents are possible on the shoreface and continental slope, where slopes commonly exceed 0.02. Over slopes less than about 0.01, shear associated with the gravity current alone will not be sufficient to generate turbulence. As sediment settles out over slopes less than 0.01, the down-slope pressure gradient driving the gravity current is simultaneously reduced, keeping the shear below that necessary to generate turbulence. This is why gravity currents initiated near river mouths typically dissipate if they move out across a relatively flat shelf.

33.4 Summary and conclusions

In general, models appear to do good work on reproducing the planetary and tidal bottom boundary layer, at least for the homogeneous case, but in most of the numerical models this is dependent on using the logarithmic layer as the bottom boundary condition, which implies assuming roughness lengths or drag coefficients that might be very different from those in nature. When the water column is stratified, a successful description of the planetary and tidal bottom boundary layer will depend on the quality of our turbulence-closure scheme representing the eddy viscosity.

It is apparent that the shape of the tidal bottom boundary layer is of great importance for the efficiency of the tidal currents regarding producing vertical mixing (Simpson and Sharples, 1994) and the capability of resuspending sediments. The clockwise tidal currents appear to be more efficient at producing water-column mixing than the anti-clockwise currents; this is due to the fact that the bottom boundary layer for clockwise currents is greater than that for anti-clockwise currents. Conversely, the concentration of the shear near the bottom boundary might make the anti-clockwise currents more effective at resuspending sediment.

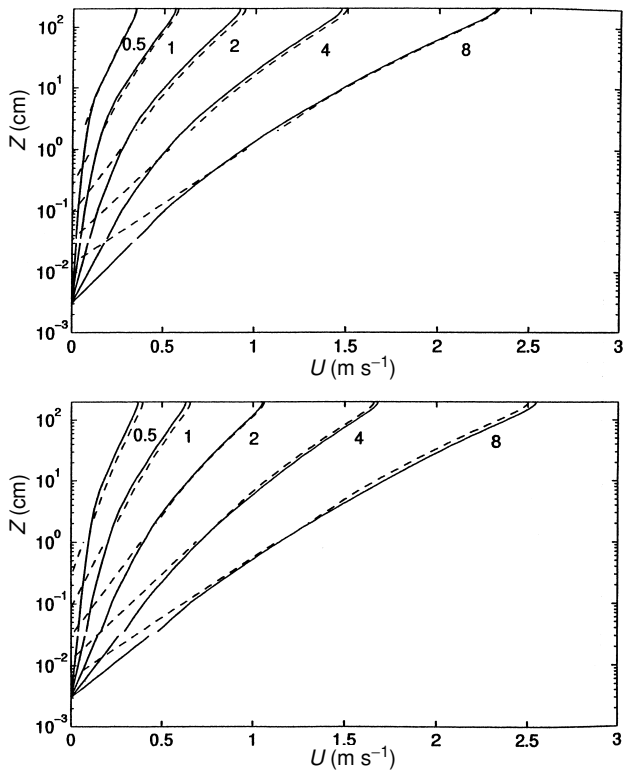

Fig. 33.8. A comparison of phase-averaged resolved solutions (solid curves) with the parameterized solutions (dashed curves) using the apparent roughness in the law of the wall. The oscillatory parameters are $\omega = 9.6\,\mathrm{s}^{-1}$ and $z_0 = 30.06 \times 10^{-5}$ m. (a) $\phi = 0°$, (b) $\phi = 90°$. The short straight lines (solid) and the longer lines (dashed) are law-of-the-wall plots in which z_0 and z_{0a}, respectively, are denoted by the $u = 0$ intercepts. From Mellor (2002).

Although the most common method for including the effect of waves in the bottom boundary layer is to use a version of the method used in Section 33.1, it is apparent that this is not the best approach with which to attack the problem. These methods are based on the calculation of the bottom drag coefficient using an unaltered law of the wall and altering only the roughness z_0, by using an apparent roughness $k_{bc}/30$ (see Eq. (33.56)). The result of this sort of parameterization compared with resolved simulations is shown in Fig. 33.8 (Mellor, 2002). The parameterized and resolved solutions closely resemble each other, except at small values of z. It is in this region of low z values that part of the solution is not available, so these problems near the boundary could be of importance for sediment transport. A greater problem is that the calculations can be unstable if the matching point z_r is less than the apparent roughness ($k_{bc}/30$).

The Mellor (2002) parameterization appears to be a better model to use and has the advantages of being simple to apply and that it is plugged in straight into the closure scheme, with very little computational cost. An extra advantage of the Mellor (2002) approach is that the wave shear production P_w can be useful dissipation information for wave models.

Beside the effects of waves and currents, also sediment affects the hydrodynamics of the bottom boundary layer, mainly in three ways: by forming bottom roughness, damping turbulence, and creating a down-slope pressure gradient. The presence of suspended sediment stabilizes the bottom boundary layer, enhancing the shear produced by a given stress and causing the slope of the observed logarithmic profile to overestimate the friction velocity. Suspended sediment can ultimately provide so much stabilizing buoyancy that turbulence is shut down and internal waves appear. Across slopes greater than about 0.02, sediment gravity currents have the potential of self-accelerating due to additional suspension from the bed in response to stress generated by the gravity current itself.